

# CuInSe<sub>2</sub> Quantum Dots Hybrid Hole Transfer Layer for Halide Perovskite Photodetectors

Ruiqi Guo,<sup>†</sup> Fei Huang,<sup>†</sup> Kaibo Zheng,<sup>‡,§</sup> Tönu Pullerits,<sup>‡</sup> and Jianjun Tian<sup>\*,†</sup>

<sup>†</sup>Institute for Advanced Materials and Technology, University of Science and Technology Beijing, Beijing 100083, China

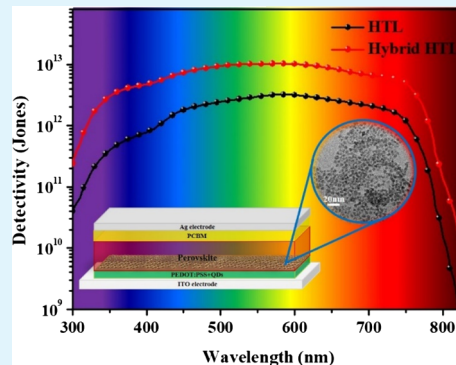
<sup>‡</sup>Department of Chemical Physics and NanoLund, Lund University, Box 124, 22100 Lund, Sweden

<sup>§</sup>Department of Chemistry, Technical University of Denmark, DK-2800 Kongens Lyngby, Denmark

## Supporting Information

**ABSTRACT:** A novel hybrid hole transport layer (HTL) of CuInSe<sub>2</sub> quantum dots (QDs)/poly(3,4-ethylenedioxythiophene):poly(styrenesulfonate) (PEDOT:PSS) was developed to enhance the performance of halide metal perovskite (MAPbI<sub>3</sub>)-based photodetectors. The introduction of CuInSe<sub>2</sub> QDs not only improved the wettability of the PEDOT:PSS HTL for the growth of perovskite crystals but also facilitated the transportation of holes from the perovskite to the HTL. As a result, both responsivity and detectivity of the device were increased dramatically by CuInSe<sub>2</sub> QDs hybrid HTL, showing excellent photoresponsivity of 240 mA/W, larger ratio of photocurrent density to dark current density of  $4.1 \times 10^6$ , fast on-off switching properties of  $<0.02$  s, and remarkable detectivity values of  $1.02 \times 10^{13}$  Jones at 580 nm and above  $5.01 \times 10^{12}$  Jones over the visible light region without an external bias voltage. In addition, the photodetectors also showed excellent thermal stability in the range of 10–110 °C. Therefore, a unique design idea of a hole transport material would be an anticipated direction for efficient halide metal perovskite-based devices.

**KEYWORDS:** quantum dots, CuInSe<sub>2</sub> QDs, PEDOT:PSS, perovskite, photodetector



## 1. INTRODUCTION

Photodetectors can convert photons of different energies into electrical signals,<sup>1,2</sup> which are widely used in visible light cameras, optical communications, and medicine.<sup>3–6</sup> Till date, a large variety of semiconductor materials have been developed as photoactive layers for photodetectors, such as Si, quantum dots (QDs), metal-oxide nanocomposites, carbon nanotubes, and conjugated polymers.<sup>7–12</sup> However, they always required a complicated preparation process involving high cost. There is still an urgent need to seek some materials to achieve the high detectivity photodetector using a cost-efficient fabrication process. Organic–inorganic hybrid perovskite materials with a classical formula of ABX<sub>3</sub> [A = CH<sub>3</sub>NH<sub>3</sub><sup>+</sup> (MA), NH=CHNH<sub>3</sub><sup>+</sup> (FA); B = Pb<sup>2+</sup>, Sn<sup>2+</sup>; X = Cl<sup>-</sup>, Br<sup>-</sup>, and I<sup>-</sup>] have attracted tremendous attention as promising building blocks for a wide range of opto-electronic devices, such as solar cells,<sup>13–17</sup> light-emitting diodes,<sup>18–21</sup> and photocatalytical devices.<sup>22</sup> Recently, the application of perovskite materials in photodetectors has become a new landscape because of their strong optical absorption coefficient, a suitable direct band gap, large defect tolerance, and a long carrier diffusion length.<sup>13–16</sup> In addition, the reported perovskite photodetectors not only can get remarkable highly responsivity and detectivity within the visible light region but also possess higher intrinsic charge-carrier mobility compared with the conventional photodetector materials.<sup>23,24</sup>

A typical perovskite photodetector consists of transport oxide conductor (TOC)/hole transport layer (HTL)/perovskite/electron transport layer (ETL)/metal electrode. Poly(3,4-ethylenedioxythiophene):poly(styrenesulfonate) (PEDOT:PSS) is usually selected as one of the hole transport materials (HTMs) attributed to good light transmittance, heat resistance, and environmental friendliness. However, the poor hole transportation and wettability of PEDOT:PSS restrict the potential performance of the perovskite-based photodetectors. Therefore, an alternative HTM needs to be developed. In our previous work,<sup>11</sup> we found that CuInSe<sub>2</sub> QDs as p-type materials could not only perfectly match the band structure with organic HTM but also act as the active material to produce excitons to improve the detectivity of photodetectors. It suggested that the introduction of CuInSe<sub>2</sub> QDs in the HTL would be helpful for transferring holes to further improve the performance of the perovskite-based photodetectors.

Here, we designed a novel hybrid HTL via combining CuInSe<sub>2</sub> QDs and PEDOT:PSS for organic–inorganic halide perovskite photodetectors. CuInSe<sub>2</sub> QDs could serve as nucleation centers for the growth of perovskite crystals. The energy band structure of CuInSe<sub>2</sub> QDs and PEDOT:PSS were

Received: August 11, 2018

Accepted: September 25, 2018

Published: September 25, 2018

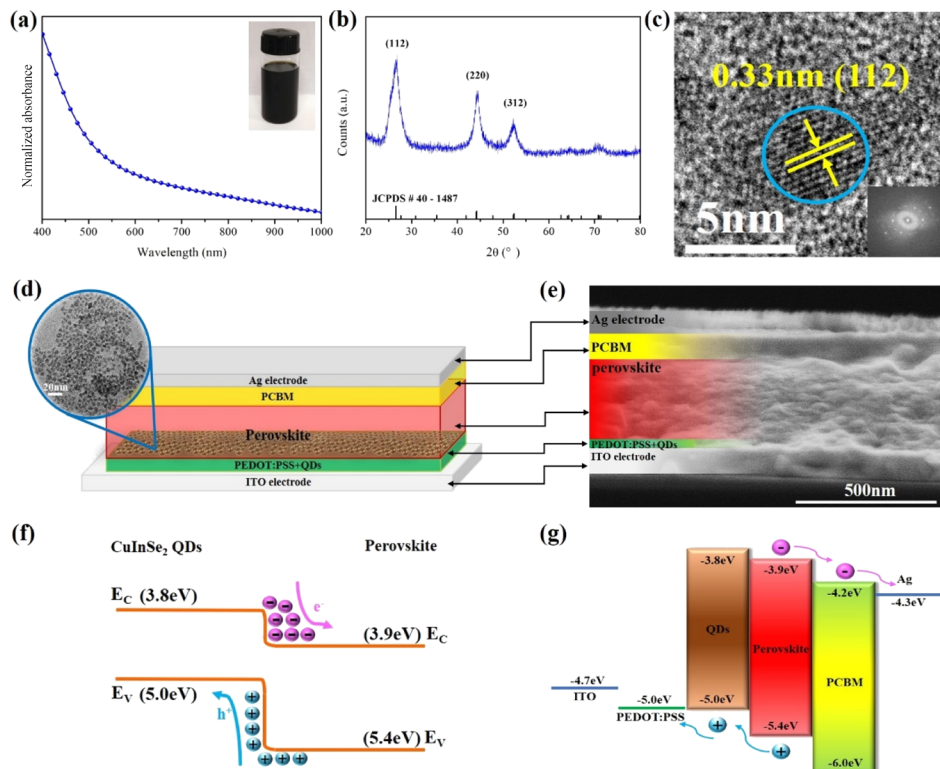


**Figure 1.** (a) Absorption spectra of CuInSe<sub>2</sub> QDs; the inset diagram shows the picture of CuInSe<sub>2</sub> QD solution. (b) XRD patterns of CuInSe<sub>2</sub> QDs. (c) HRTEM micrograph of CuInSe<sub>2</sub> QDs. (d) Schematic structure (with TEM image of CuInSe<sub>2</sub> QDs) and (e) cross-sectional SEM image of the perovskite photodetector. (f) Energy band diagram of the CuInSe<sub>2</sub> QDs/MAPbI<sub>3</sub> perovskite. (g) The HOMO and lowest unoccupied molecular orbital energy levels of each layer in the photodetector.

perfectly matched to facilitate the derivation of holes. In addition, as a near-infrared absorbing material, CuInSe<sub>2</sub> QDs were considered to enhance the light harvesting of the devices. As a result, the perovskite photodetector using the hybrid HTL presented faster on–off switching properties less than <0.02 s, satisfactory responsivity of over 240 mA/W, and decent detectivity of  $1.02 \times 10^{13}$  Jones under an illumination density of 100 mW cm<sup>-2</sup>.

## 2. RESULTS AND DISCUSSION

We designed a hybrid HTL consisting of PEDOT:PSS and CuInSe<sub>2</sub> QDs and fabricated CH<sub>3</sub>NH<sub>3</sub>PbI<sub>3</sub> (MAPbI<sub>3</sub>) perovskite photodetectors. Figure 1a shows the absorption spectra of CuInSe<sub>2</sub> QD solution prepared by the hot-injection synthesis according to our previous work.<sup>11</sup> The absorption onset of the CuInSe<sub>2</sub> QDs can extend to 1000 nm; the inset diagram displays the color of CuInSe<sub>2</sub> QDs. Figure 1b displays the X-ray diffraction (XRD) patterns of CuInSe<sub>2</sub> QDs, indicating the chalcopyrite structure corresponding to JCPDS#40-1487. In high-resolution transmission electron microscopy (HRTEM), the clear lattice stripes with the atomic spacing correlated to the (112) plane of CuInSe<sub>2</sub> QDs phase can also be observed, as shown in Figure 1c. This demonstrates the good crystallinity of CuInSe<sub>2</sub> QDs. The responsivity of the photodetectors with different perovskite precursor concentrations were studied, as shown in Figure S1, indicating that the device shows the best performance with 0.3 M precursor solution. Hence, the MAPbI<sub>3</sub> perovskite layer was fabricated from the precursor solution of CH<sub>3</sub>NH<sub>3</sub>I (MAI) and PbI<sub>2</sub> with an additive of 2-methoxyethanol. The absorption onset of the perovskite layer is 780 nm as shown in Figure S2a, indicating a range of whole

visible wavelengths. The structure of perovskite was verified using XRD and scanning electron microscopy (SEM), as shown in Figure S2b,c. The configuration of TOC/hybrid HTL/MAPbI<sub>3</sub>/ETL/Ag is shown in Figure 1d. The mixture solution of CuInSe<sub>2</sub> QDs and PEDOT:PSS was spin-coated on TOC of the indium tin oxide (ITO) substrate. The perovskite film was then deposited on this hybrid HTL via spin-coating the precursor solution, and then the wet film was annealed at 100 °C for 30 min. The ETL was made of phenyl-C<sub>61</sub>-butyric acid methyl ester (PC<sub>61</sub>BM). Finally, a silver (Ag) layer was deposited on the top electrode by thermal evaporation in vacuum. The cross-sectional SEM image of the photodetector is shown in Figure 1e, where the boundary of the hybrid HTL is difficult to distinguish. This indicates the good connection between the hybrid HTL and the perovskite layers, where the hybrid HTL could possibly merge into the halide perovskite layer. On the contrary, the boundary of the PEDOT:PSS layer without QDs in the device is clear, as shown in Figure S3. Unbelievably, the thickness of the perovskite changes significantly from 170 nm (HTL-based device) to 300 nm (hybrid HTL-based device). This indicates that the hybrid HTL is more conducive to the growth of perovskite. The energy band alignment of each layer in the photodetector structure is shown in Figure 1f,g. Under illumination, the electron–hole pairs are generated in the perovskite layer and CuInSe<sub>2</sub> QDs. The holes are transferred via HTL to the ITO electrode, whereas the electrons are transferred by PCBM to the Ag electrode, forming the corresponding photocurrent. CuInSe<sub>2</sub> QDs in the hybrid HTL could serve as an electron barrier layer to prevent electron transport to the cathode electrode because of its high highest occupied molecular

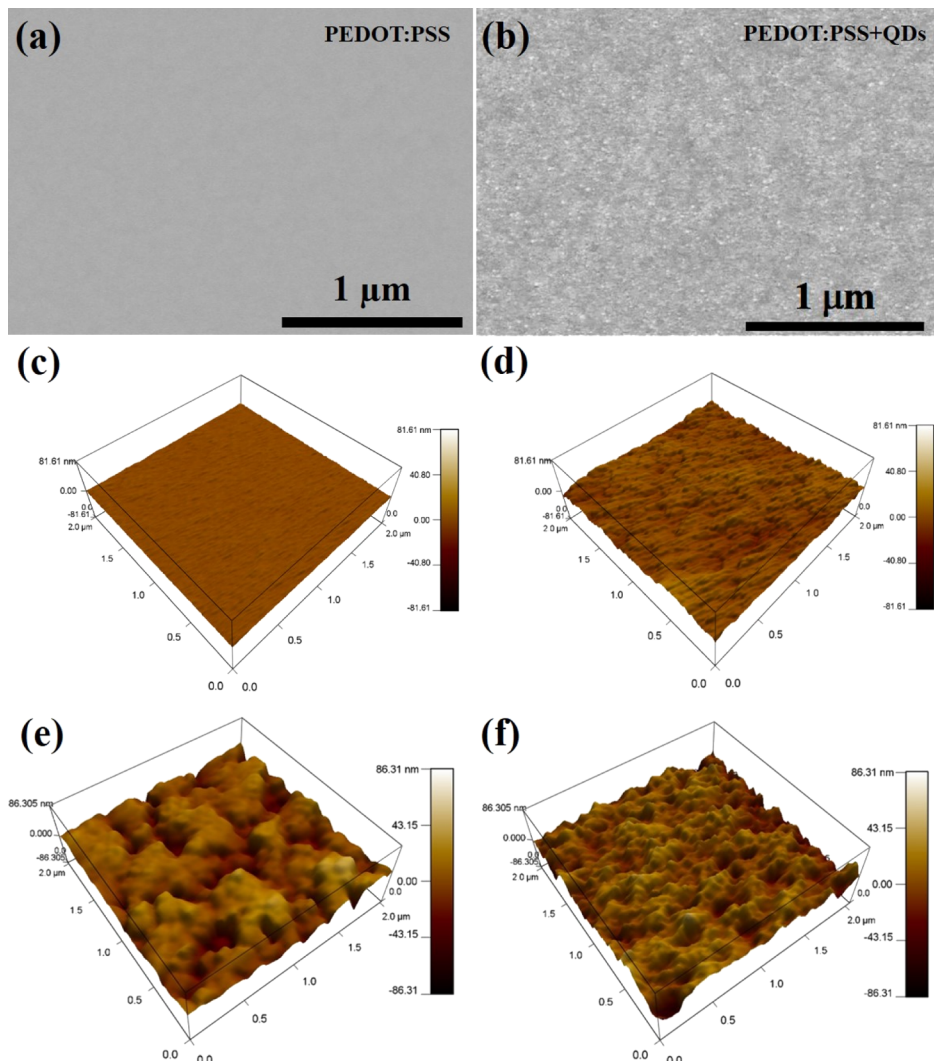


**Figure 2.** Surface SEM images of (a) PEDOT:PSS HTL and (b) PEDOT:PSS + QDs hybrid HTL. AFM three-dimensional surface morphology images of (c) PEDOT:PSS HTL and (d) PEDOT:PSS + QDs hybrid HTL. (e,f) AFM three-dimensional surface morphology images of perovskite films based on the HTL and hybrid HTL, respectively. The scan size is 2  $\mu\text{m} \times 2 \mu\text{m}$ .

orbital (HOMO) energy level. The electrons transfer to the ETL while the holes effectively collected by the hybrid HTL further reach the ITO electrode. Consequently, the photocurrent of the device in the visible region is dramatically enhanced. To verify the performance of the hybrid HTL,  $J$ - $V$  curves of the devices with the structure of ITO/HTL or hybrid HTL/Ag were tested, as shown in Figure S4. In the voltage test region, the control sample with the conventional single component HTL presents an Ohmic conduction. The resistance remains constant both in the dark and under the light. However, the device with the hybrid HTL displays the transport behavior consisting of both an Ohmic region and Child's law region, as shown in Figure S4c. This indicates that trap states still dominated the charge-carrier transportation in the low-voltage region. When the bias voltage is increased, the conduction mechanism is modulated by injection electrons. Traps are continuously filled with electrons, leading to the sudden increase of the current in the hybrid HTL-based device.

To further understand the effect of CuInSe<sub>2</sub> QDs on the HTLs, we studied the morphologies of the HTL, hybrid HTL, and perovskite layers. SEM images are shown in Figure 2a,b,

and atomic force microscopy (AFM) top views of the HTLs are shown in Figure 2c,d. It indicates the larger root-mean-square (rms) roughness of the hybrid HTL (4.44 nm) compared with that of neat HTL (1.48 nm). The high surface roughness should facilitate the formation and longitudinal growth of the perovskite layer.<sup>25</sup> This is one of the reasons for the improved photocurrent and response of the hybrid HTL detector. On the other hand, the addition of CuInSe<sub>2</sub> QDs in PEDOT:PSS could also change the grain size and surface roughness of the perovskite films. The SEM images of the perovskite films on the HTL and hybrid HTL are shown in Figure S5. When CuInSe<sub>2</sub> QDs are introduced, the grain size of the perovskite is significantly reduced, indicating that a large number of CuInSe<sub>2</sub> QDs serving as the growth pillar limit the lateral growth of perovskite. As shown in the AFM images in Figure 2e,f, the perovskite film on the neat HTL substrate shows the rms roughness of 11.8 nm, whereas smaller rms roughness (9.92 nm) can be observed on the hybrid HTL substrate. It should be attributed to the rapid crystallization of perovskite on the hybrid HTL because of high roughness, which makes the perovskite grains smaller and the perovskite film denser.

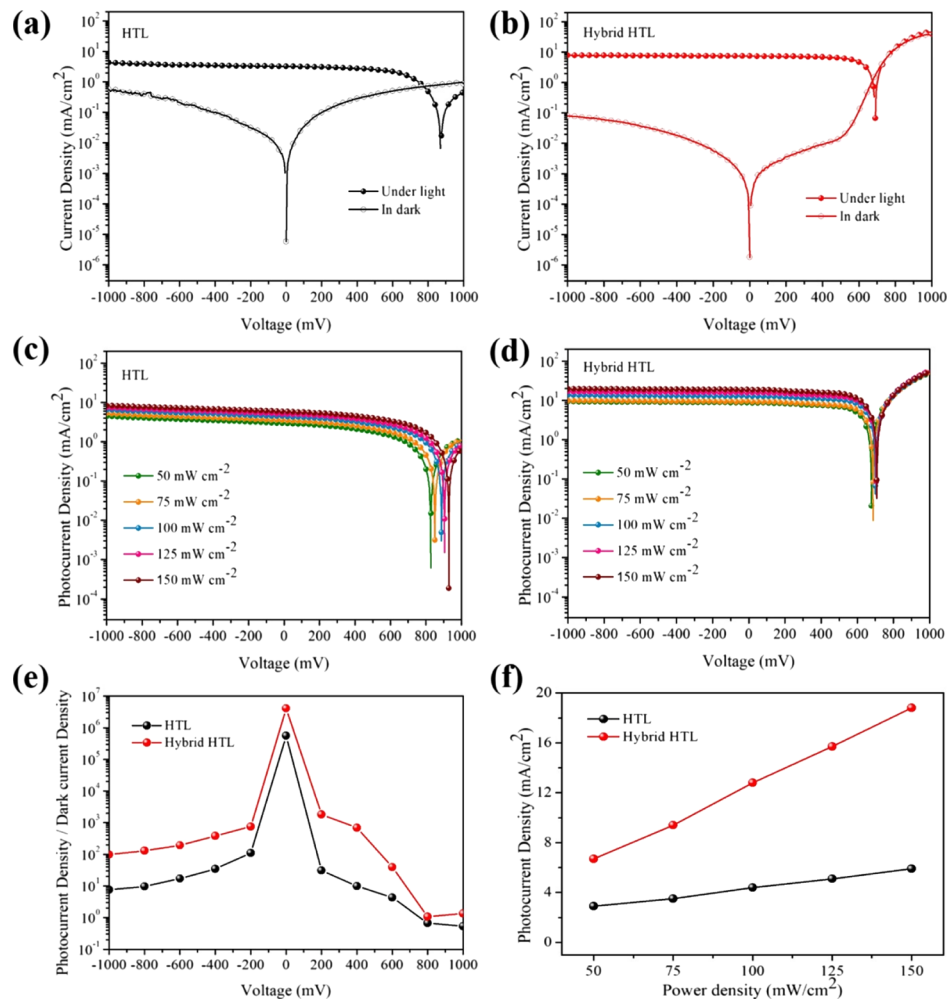


**Figure 3.** Logarithmic form of photocurrent density–voltage and dark current density–voltage curves of the (a) control sample using HTL and (b) hybrid HTL-based device.  $J$ – $V$  characteristics of the (c) control sample using HTL and (d) hybrid HTL-based device under an illumination density of 50, 75, 100, 125, and 150  $\text{mW cm}^{-2}$ . (e) Photocurrent density and dark current density ratio of two structural devices at different voltages from −1000 to 1000 mV. (f) Photocurrent density of the photodetectors under various power densities from 50 to 150  $\text{mW cm}^{-2}$  at 0 V bias voltage.

Photocurrent density and dark current density–voltage curves of the two devices with the HTL and hybrid HTL are shown in Figure 3a,b, respectively. The ratio of photocurrent density to dark current density is  $5.6 \times 10^5$  and  $4.1 \times 10^6$  for HTL and hybrid HTL devices at 0 V, respectively. Notably, the detector based on the hybrid HTL exhibits significantly higher photocurrent density and fill factor than those of the control sample, indicating the more efficient charge-carrier transport in the hybrid HTL device. Besides that, the lower dark current density can be observed in the hybrid HTL device, which manifests excellent antinoise and detection performance. In the meantime, the linear dynamic range (LDR) provides a linear relationship between the photocurrent and the light excitation intensity ( $\text{LDR} = 20 \log J_{\text{light}}/J_{\text{dark}}$ ).<sup>3,26</sup> The LDR for the hybrid HTL-based photodetector (132 dB) is much higher than that for the HTL-based device (115 dB). The light current density–voltage characteristics of the HTL and hybrid HTL structural detectors under irradiation of various power densities are shown in Figure 3c,d, respectively. It can be seen that the photocurrent densities of all detectors increase as the power density increased, indicating that both of the devices are sensitive to light. The hybrid HTL-based detector has higher current density than the HTL-structured detector under

the same condition. Figure 3e shows the ratio of photocurrent density to dark current density at different voltages by 100  $\text{mW cm}^{-2}$  illumination. The minimum dark current density and the maximum ratio of the photocurrent density to the dark current density both occur at 0 V, indicating that the device has a feasible energy band structure, and the zero-offset voltage is avoided.<sup>27</sup> We also summarized the functional relationship between the current and the power density, as displayed in Figure 3f. In general, the photocurrent density increases with the increment of the light density. The photocurrent density of the hybrid HTL-based device is higher than that of the HTL-based device. At a power density of 150  $\text{mW cm}^{-2}$ , the current density of the hybrid HTL-based device is  $18.8 \text{ mA cm}^{-2}$ , whereas that of the HTL-based device is only  $5.9 \text{ mA cm}^{-2}$ . In practical applications, the photocurrent density and light power density cannot fully show the proportional growth because of the existence of charge separation and defects. The more obvious the change occurs, the stronger the light response ability. All of the above results manifest the superior performance of the hybrid HTL-based photodetector compared to that of the HTL-based device.

The speed of photoresponse switching can characterize the sensitivity of the photodetectors.<sup>10,24,28</sup> Figure 4a–c shows the

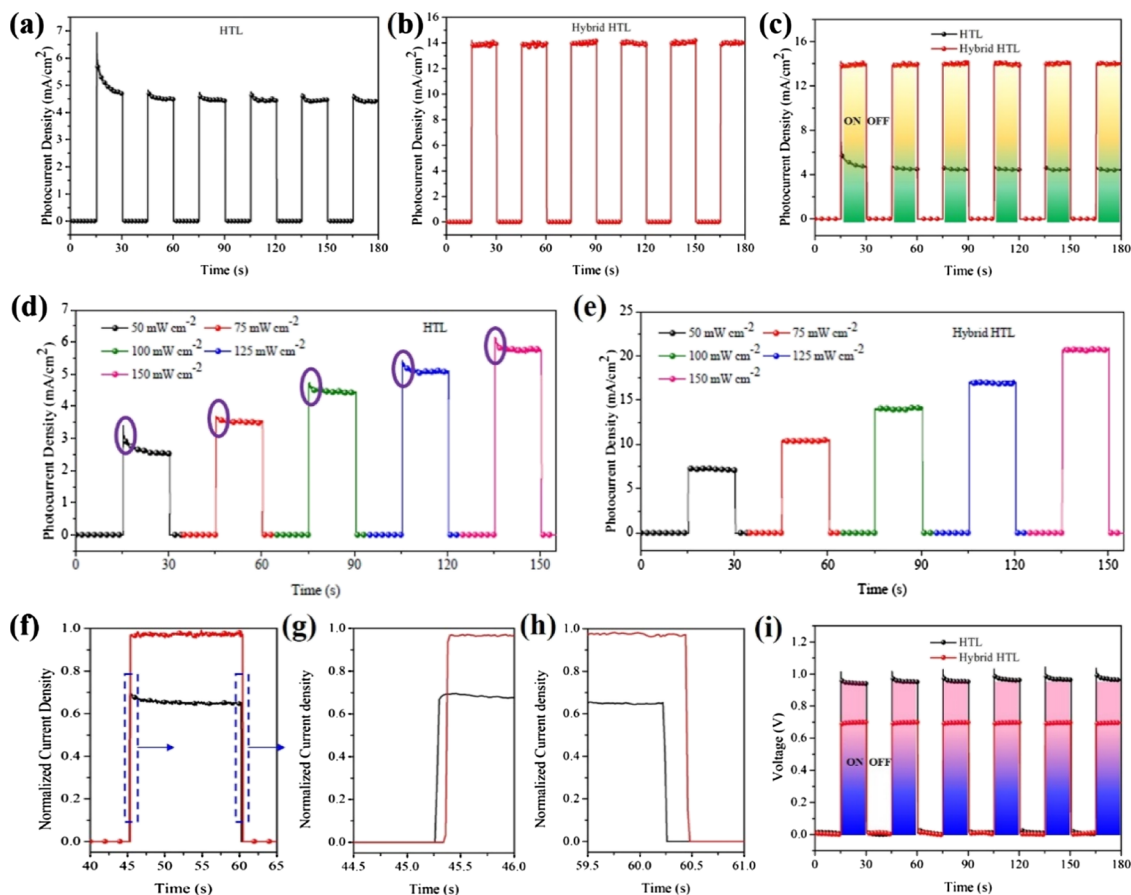


**Figure 4.** (a–c) Time-dependent photoresponse of two structural devices under 100 mW cm<sup>-2</sup> illumination and at 0 V bias voltage. (d,e) Response of current density of two structural devices under different power densities at 50, 75, 100, 125, and 150 mW cm<sup>-2</sup>. (f) Time-resolved photocurrent density of the two structural devices. (g) Rise and (h) decay times of the photodetector devices. (i) Responses of the open current voltage of the devices upon 100 mW cm<sup>-2</sup> power density measured for light-on and -off states.

temporal response of the photodetectors with the incident light (100 mW cm<sup>-2</sup>) switched on and off repeatedly. Both two devices present perfect on–off reproducibility within six-cycle tests. Clearly, the photocurrent density of the hybrid HTL-based device is 3 times more than that of the control device-based HTL. Notably, the hybrid HTL-based device can instantaneously reach equilibrium condition after initial excitation without a pronounced current drop from the maximum value of the current density observed in HTL-based detectors, as shown in Figure 4a,b. This should be attributed to the absence of trap defects in the hybrid HTL device, and the trap filling process can be negligible. We also confirm that such an initial current drop in the neat HTL-based devices cannot be mended by changing the excitation intensity, as shown in the purple area of Figure 4d, which means the trap density in conventional HTLs should be much larger than the density of the injected charges under normal excitation condition. The results from the “ON” and “OFF” transients show that the hybrid HTL-based device will soon be stable and has an ultrasensitive response speed at any light power density, as shown in Figure 4e. The detailed temporal responses of photocurrent within one illumination cycle for HTL- and hybrid HTL-based devices have been depicted in Figure 4f–h. Here, the rise time ( $t_r$ ) is defined, as the photocurrent increases from 10 to 90% of the maximum value, and the fall time ( $t_f$ ) is defined, as the photocurrent decreases from 90 to 10% regarding the peak output value.<sup>11,28</sup> Both  $t_r$

and  $t_f$  of the hybrid HTL-based photodetector (<0.02 s) are faster than those of the HTL-based photodetector (>0.04 s). Figure 4i also shows the reproducible temporal responses of the open-circuit voltage of the two kinds of devices with the same excitation condition as above. The rapid temporal response in the hybrid HTL device indicates the fast separation and extraction of photocarriers,<sup>29</sup> which can be ascribed to the high carrier mobility and the low defect density.

To evaluate the device performance, the responsivity ( $R$ ) and specific detectivity ( $D^*$ ) are calculated by the equations<sup>11,28,30,31</sup>

$$R = \frac{J_{\text{ph}}}{L_{\text{light}}} \quad (1)$$

$$D^* = R_\lambda \frac{1}{\sqrt{(2qJ_d)}} \quad (2)$$

where  $J_{\text{ph}}$  is the photocurrent density,  $L_{\text{light}}$  is the incident light density,  $R_\lambda$  is the photoresponsivity,  $q$  is the elementary charge, and  $J_d$  is the dark current density.<sup>11,26,28</sup> In general, the wavelength-dependent photoresponsivity follows the absorption spectra of the perovskite film (Figure S2). The hybrid HTL-based device has a much higher  $R$  with the maximum value >240 mA/W than the control detector with the maximum value around 135 mA/W, as shown in Figure 5a. To testify whether the enhancement of the photoresponsivity

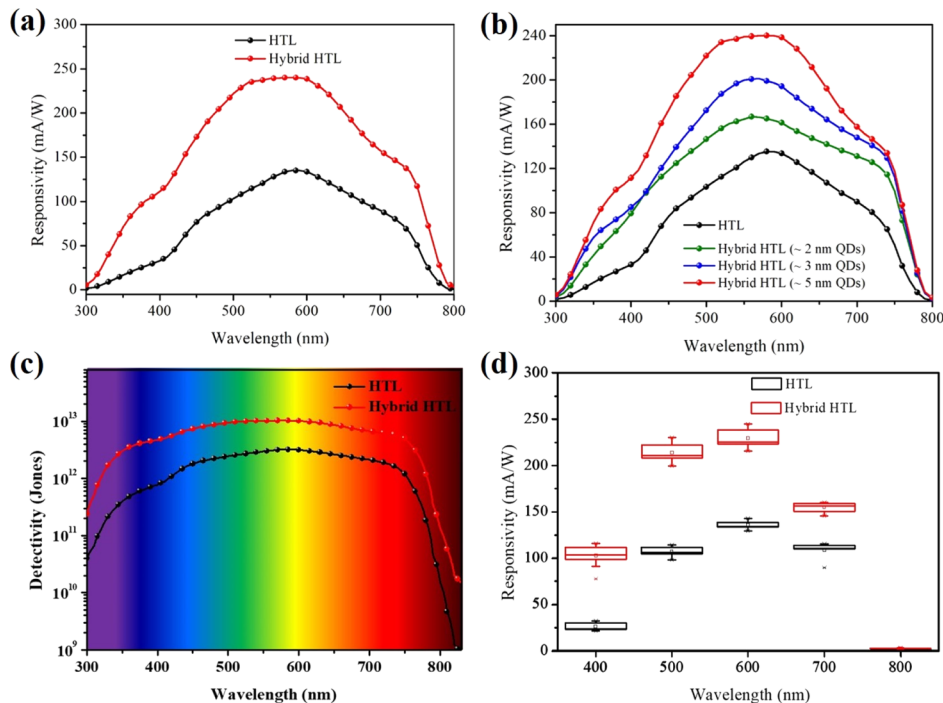


**Figure 5.** (a) Responsivity and (c) specific detectivity of the photodetectors assembled with hybrid HTL or HTL, calculated at 0 V bias voltage. (b) Four devices of different HTLs with a wavelength of illumination from 300 to 800 nm. (d) Summary of the responsivity of 10 photodetectors with 2 structures.

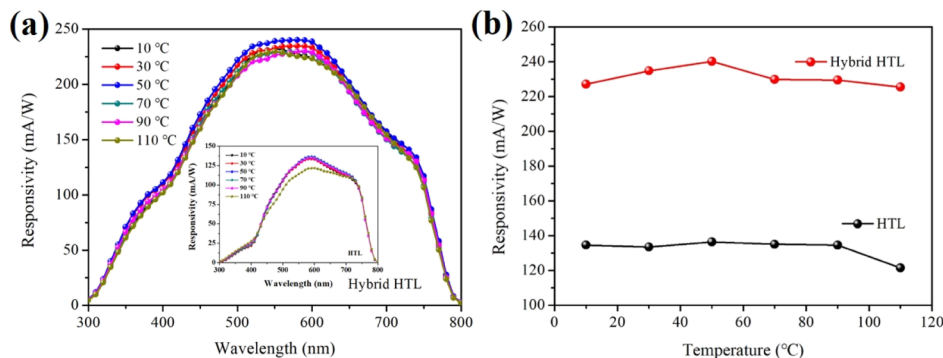


**Figure 6.** (a) Responsivity of the devices with the hybrid HTL and HTL after heating at different temperatures (10, 30, 50, 70, 90, and 110 °C) for 10 min. (b) Comparison diagram of the thermal stability of the hybrid HTL and HTL devices at 580 nm.

is due to the additional light absorption from CuInSe<sub>2</sub> QDs in this photodetector, we studied the performance of a series of devices based on CuInSe<sub>2</sub> QDs of various sizes, as shown in Figure 5b. The size of QDs was controlled by the synthesis temperature (120–200 °C). Obviously, compared with the HTL-based device,  $R$  of the hybrid HTL-based devices increases to varying degrees with the increase of the QD size. The  $R$  values are 135 mA/W (HTL-based device), 165 mA/W ( $\sim$ 2 nm QDs hybrid HTL-based device), 191 mA/W ( $\sim$ 3 nm QDs hybrid HTL-based device), and 240 mA/W ( $\sim$ 5 nm QDs hybrid HTL-based device) at 580 nm. The  $\sim$ 5 nm CuInSe<sub>2</sub> QDs hybrid HTL-based device has the highest light response ability. This result demonstrates that the enhancement of performance of the detectors may be partially from the contribution of light harvesting of QDs. Certainly, another figure of merit is  $D^*$ ; higher  $D^*$  indicates that the device has higher photosensitivity in the levels of signal and noise.<sup>8</sup> It can be evaluated, as presented in eq 2. Figure 5c shows the specific  $D^*$  of the devices within 300–800 nm, calculated at 0 V bias

voltage.  $D^*$  of the hybrid HTL-based photodetector is much higher than that of the HTL-based device over the visible light region at 0 V. It can also be observed that the largest  $D^*$  of the control device is only  $3.03 \times 10^{12}$  Jones (1 Jones = 1 cm Hz<sup>1/2</sup> W<sup>-1</sup>) and that of the hybrid HTL-based device is remarkably above  $5.01 \times 10^{12}$  Jones over the visible light region. The maximum  $D^*$  of the hybrid HTL-based device reaches  $1.02 \times 10^{13}$  Jones located at 580 nm. In addition, we also compared with the reported perovskite (MAPbI<sub>3</sub>)-based photodetectors, as shown in Table S1. It is found that the performance of this detector is better than that of the reported devices. Figure 5d shows the  $R$  values of 10 photodetectors for 2 structural devices, which further confirm the better performance of the hybrid HTL-based devices over the wavelength from 300 to 800 nm.

To study the thermal stability of the photodetectors, the devices were heated at different temperatures. Figure 6a illustrates the responsivity of the HTL- and hybrid HTL-based devices after heating at different temperatures for 10 min.

When the temperature slightly increased to 50 °C, the responsivity of the two kinds of devices all increased accordingly. It presumes that the defects of the active layer are fast filled by the carrier in a hot environment. On further increasing the temperature, the responsivity has a minor change until the temperature reached 90 °C. When the devices were heated at 110 °C for 10 min, the response of the HTL-based devices decreased by 9.9%, whereas the response of the hybrid HTL-based detectors only decreased by 0.7%. Figure 6b compares the responsivity of the detectors based on the hybrid HTL and HTL at 580 nm after heating at different temperatures for 10 min. Compared with the HTL-based devices, the change of responsivity is almost negligible for the hybrid HTL-based devices. Table 1 summarizes the decrease

**Table 1. Decrease Rate of Responsivity of the HTL- or Hybrid HTL-Based Devices at Different Wavelengths after Heating at 110 °C for 10 min**

photodetectors	rate				
	optical wave				
	400 nm	500 nm	600 nm	700 nm	800 nm
HTL-based device	16.0%	12.8%	8.7%	0.72%	25%
hybrid HTL-based device	1.3%	1.1%	0.2%	1.19%	5.95%

rate of responsivity of the devices under different conditions. It is obvious that the hybrid HTL-based detector exhibits better thermal stability than the control device.

### 3. CONCLUSIONS

The novel hybrid HTM of CuInSe<sub>2</sub> QDs and PEDOT:PSS for enhancement performance of MAPbI<sub>3</sub> perovskite-based photodetectors was successfully designed and fabricated. The tentative explanations about the introduction of CuInSe<sub>2</sub> QDs in PEDOT:PSS to form a hybrid HTL would be the following: (1) the energy band structure of CuInSe<sub>2</sub> QDs and PEDOT:PSS was perfectly matched to facilitate the extraction of holes from the perovskite; (2) CuInSe<sub>2</sub> QDs increased the surface roughness of PEDOT:PSS that would serve as the nucleation centers for the growth of perovskite crystals; and (3) the excellent light harvesting of CuInSe<sub>2</sub> QDs may be helpful for the increase of charge collection of the active layer (HTM + perovskite). The resulting hybrid HTL-based device was superior to the control device in the field of larger ratio of photocurrent density to dark current density ( $4.1 \times 10^6$ ), broader LDR (132 dB), faster on-off switching properties (<0.02 s), higher photoresponsivity (240 mA/W), and larger detectivity ( $\sim 1.02 \times 10^{13}$  Jones). Therefore, CuInSe<sub>2</sub> QDs would be an effective hybrid agent mixed with PEDOT:PSS to realize a high-performance photodetector. In addition, the excellent thermal stability ( $\sim 110$  °C) of the hybrid HTL-based photodetector was well-demonstrated. This work is an unprecedented attempt in the field of perovskite photodetectors, which is also meaningful for the perovskite-based photoelectric devices, including solar cells and light emission diodes.

### ASSOCIATED CONTENT

#### Supporting Information

The Supporting Information is available free of charge on the ACS Publications website at DOI: [10.1021/acsami.8b13777](https://doi.org/10.1021/acsami.8b13777).

Experimental details of the manufacturing procedures, additional supplementary figures, device characterization, and device statistics ([PDF](#))

### AUTHOR INFORMATION

#### Corresponding Author

\*E-mail: [tianjianjun@mater.ustb.edu.cn](mailto:tianjianjun@mater.ustb.edu.cn).

#### ORCID

Kaibo Zheng: [0000-0002-7236-1070](#)

Tönu Pullerits: [0000-0003-1428-5564](#)

Jianjun Tian: [0000-0002-4008-0469](#)

#### Notes

The authors declare no competing financial interest.

### ACKNOWLEDGMENTS

This work was supported by the National Science Foundation of China (S1774034, S1772026, and S1611130063), the Beijing Natural Science Foundation (2182039), Fundamental Research Funds for the Central Universities (FRF-TP-17-030A1, FRF-TP-17-083A1, FRF-TP-17-082A1, and TW2018010), and Project funded by the China Postdoctoral Science Foundation (2017M620611 and 2018M630068). K.Z. acknowledges the support by the Danish Council for Independent Research no. 7026-0037B and the Swedish Research Council no. 2017-05337.

### REFERENCES

- (1) Saran, R.; Curry, R. J. Lead sulphide nanocrystal photodetector technologies. *Nat. Photonics* **2016**, *10*, 81–92.
- (2) Konstantatos, G.; Sargent, E. H. Nanostructured materials for photon detection. *Nat. Nanotechnol.* **2010**, *5*, 391–400.
- (3) Tian, W.; Zhou, H.; Li, L. Hybrid Organic-Inorganic Perovskite Photodetectors. *Small* **2017**, *13*, 1702107.
- (4) Cao, F.; Liao, Q.; Deng, K.; Chen, L.; Li, L.; Zhang, Y. Novel perovskite/TiO<sub>2</sub>/Si trilayer heterojunctions for high-performance self-powered ultraviolet-visible-near infrared (UV-Vis-NIR) photodetectors. *Nano Res.* **2018**, *11*, 1722–1730.
- (5) Siontas, S.; Li, D.; Liu, P.; Aujla, S.; Zaslavsky, A.; Pacifici, D. Low-Temperature Operation of High-Efficiency Germanium Quantum Dot Photodetectors in the Visible and Near Infrared. *Phys. Status Solidi A* **2018**, *215*, 1700453.
- (6) de Arquer, F. P. G.; Gong, X.; Sabatini, R. P.; Liu, M.; Kim, G.-H.; Sutherland, B. R.; Voznyy, O.; Xu, J.; Pang, Y.; Hoogland, S.; Sinton, D.; Sargent, E. Field-emission from quantum-dot-in-perovskite solids. *Nat. Commun.* **2017**, *8*, 14757.
- (7) Oertel, D. C.; Bawendi, M. G.; Arango, A. C.; Bulović, V. Photodetectors based on treated CdSe quantum-dot films. *Appl. Phys. Lett.* **2005**, *87*, 213505.
- (8) Ren, Z.; Sun, J.; Li, H.; Mao, P.; Wei, Y.; Zhong, X.; Hu, J.; Yang, S.; Wang, J. Bilayer PbS Quantum Dots for High-Performance Photodetectors. *Adv. Mater.* **2017**, *29*, 1702055.
- (9) Huo, N.; Gupta, S.; Konstantatos, G. MoS<sub>2</sub>-HgTe Quantum Dot Hybrid Photodetectors beyond 2 μm. *Adv. Mater.* **2017**, *29*, 1606576.
- (10) Wei, Y.; Ren, Z.; Zhang, A.; Mao, P.; Li, H.; Zhong, X.; Li, W.; Yang, S.; Wang, J. Hybrid Organic/PbS Quantum Dot Bilayer Photodetector with Low Dark Current and High Detectivity. *Adv. Funct. Mater.* **2018**, *28*, 1706690.
- (11) Guo, R.; Shen, T.; Tian, J. Broadband hybrid organic/CuInSe<sub>2</sub> quantum dot photodetectors. *J. Mater. Chem. C* **2018**, *6*, 2573–2579.
- (12) Clifford, J. P.; Konstantatos, G.; Johnston, K. W.; Hoogland, S.; Levina, L.; Sargent, E. H. Fast, sensitive and spectrally tuneable colloidal-quantum-dot photodetectors. *Nat. Nanotechnol.* **2009**, *4*, 40–44.

- (13) Fei, C.; Guo, L.; Li, B.; Zhang, R.; Fu, H.; Tian, J.; Cao, G. Controlled growth of textured perovskite films towards high performance solar cells. *Nano Energy* **2016**, *27*, 17–26.
- (14) Li, B.; Li, M.; Fei, C.; Cao, G.; Tian, J. Colloidal engineering for monolayer  $\text{CH}_3\text{NH}_3\text{PbI}_3$  films toward high performance perovskite solar cells. *J. Mater. Chem. A* **2017**, *5*, 24168–24177.
- (15) Li, B.; Fei, C.; Zheng, K.; Qu, X.; Pullerits, T.; Cao, G.; Tian, J. Constructing water-resistant  $\text{CH}_3\text{NH}_3\text{PbI}_3$  perovskite films via coordination interaction. *J. Mater. Chem. A* **2016**, *4*, 17018–17024.
- (16) Li, M.; Li, B.; Cao, G.; Tian, J. Monolithic  $\text{MAPbI}_3$  films for high-efficiency solar cells via coordination and a heat assisted process. *J. Mater. Chem. A* **2017**, *5*, 21313–21319.
- (17) Shao, Y.; Xiao, Z.; Bi, C.; Yuan, Y.; Huang, J. Origin and elimination of photocurrent hysteresis by fullerene passivation in  $\text{CH}_3\text{NH}_3\text{PbI}_3$  planar heterojunction solar cells. *Nat. Commun.* **2014**, *5*, 5784.
- (18) Wu, J.-Y.; Chun, Y. T.; Li, S.; Zhang, T.; Wang, J.; Shrestha, P. K.; Chu, D. Broadband MoS<sub>2</sub> Field-Effect Phototransistors: Ultra-sensitive Visible-Light Photoresponse and Negative Infrared Photoresponse. *Adv. Mater.* **2018**, *30*, 1705880.
- (19) Chen, Z.; Zhang, C.; Jiang, X.-F.; Liu, M.; Xia, R.; Shi, T.; Chen, D.; Xue, Q.; Zhao, Y.-J.; Su, S.; Yip, H.-L.; Cao, Y. High-Performance Color-Tunable Perovskite Light Emitting Devices through Structural Modulation from Bulk to Layered Film. *Adv. Mater.* **2017**, *29*, 1603157.
- (20) Stranks, S. D.; Snaith, H. J. Metal-halide perovskites for photovoltaic and light-emitting devices. *Nat. Nanotechnol.* **2015**, *10*, 391–402.
- (21) Zhao, L.; Gao, J.; Lin, Y. L.; Yeh, Y.-W.; Lee, K. M.; Yao, N.; Loo, Y.-L.; Rand, B. P. Electrical Stress Influences the Efficiency of  $\text{CH}_3\text{NH}_3\text{PbI}_3$  Perovskite Light Emitting Devices. *Adv. Mater.* **2017**, *29*, 1605317.
- (22) Zhang, W.; Chen, Y.; Wang, X.; Yan, X.; Xu, J.; Zeng, Z. Formation of n-n type heterojunction-based tin organic-inorganic hybrid perovskite composites and their functions in the photocatalytic field. *Phys. Chem. Chem. Phys.* **2018**, *20*, 6980–6989.
- (23) Ji, C.; Wang, P.; Wu, Z.; Sun, Z.; Li, L.; Zhang, J.; Hu, W.; Hong, M.; Luo, J. Inch-Size Single Crystal of a Lead-Free Organic-Inorganic Hybrid Perovskite for High-Performance Photodetector. *Adv. Funct. Mater.* **2018**, *28*, 1705467.
- (24) Xu, W.; Guo, Y.; Zhang, X.; Zheng, L.; Zhu, T.; Zhao, D.; Hu, W.; Gong, X. Room-Temperature-Operated Ultrasensitive Broadband Photodetectors by Perovskite Incorporated with Conjugated Polymer and Single-Wall Carbon Nanotubes. *Adv. Funct. Mater.* **2018**, *28*, 1705541.
- (25) Kim, Y. Y.; Park, E. Y.; Yang, T.-Y.; Noh, J. H.; Shin, T. J.; Jeon, N. J.; Seo, J. Fast two-step deposition of perovskite via mediator extraction treatment for large-area, high-performance perovskite solar cells. *J. Mater. Chem. A* **2018**, *6*, 12447–12454.
- (26) de Arquer, F. P. G.; Armin, A.; Meredith, P.; Sargent, E. H. Solution-processed semiconductors for next-generation photodetectors. *Nat. Rev. Mater.* **2017**, *2*, 16100.
- (27) Altin, E.; Hostut, M.; Ergun, Y. Dark current and optical properties in asymmetric GaAs/AlGaAs staircase-like multiquantum well structure. *Infrared Phys. Technol.* **2013**, *58*, 74–79.
- (28) Bai, H.; Shen, T.; Tian, J. An air-stable ultraviolet photodetector based on mesoporous TiO<sub>2</sub>/spiro-OMeTAD. *J. Mater. Chem. C* **2017**, *5*, 10543–10548.
- (29) Yang, B.; Zhang, F.; Chen, J.; Yang, S.; Xia, X.; Pullerits, T.; Deng, W.; Han, K. Ultrasensitive and Fast All-Inorganic Perovskite-Based Photodetector via Fast Carrier Diffusion. *Adv. Mater.* **2017**, *29*, 1703758.
- (30) Shen, T.; Li, B.; Zheng, K.; Pullerits, T.; Cao, G.; Tian, J. Surface Engineering of Quantum Dots for Remarkably High Detectivity Photodetectors. *J. Phys. Chem. Lett.* **2018**, *9*, 3285–3294.
- (31) Cheng, W.; Tang, L.; Xiang, J.; Ji, R.; Zhao, J. An extreme high-performance ultraviolet photovoltaic detector based on a ZnO nanorods/phenanthrene heterojunction. *RSC Adv.* **2016**, *6*, 12076–12080.